

Article

Modeling and Parameterization of the Evaporation and Thermal Decomposition of an Iron(III) Nitrate Nonahydrate/Ethanol Droplet for Flame Spray Pyrolysis

Praveen Narasu and Eva Gutheil *

Interdisciplinary Center for Scientific Computing, Heidelberg University, 69120 Heidelberg, Germany; praveen.narasu@iwr.uni-heidelberg.de

* Correspondence: gutheil@iwr.uni-heidelberg.de

Abstract: Flame spray pyrolysis (FSP) is a promising approach to generate nanoparticles from precursor solutions, where the convective droplet heating and evaporation of the single precursor solution droplet play a key role. Depending on the precursor solution under consideration, reactions inside the liquid may occur. The present numerical study concerns the heating, evaporation, and thermal decomposition of single droplets of iron(III) nitrate nonahydrate (INN) and ethanol at an initial temperature of 293.15 K in hot convective air at atmospheric pressure. If the ambience is below the thermal decomposition temperature (T_{th}) of the INN, iron nitrate particles are directly formed inside the particle, whereas at ambient temperatures beyond T_{th} , the iron nitrate thermally decomposes into gaseous Fe_2O_3 and N_2O_5 . Vaporization and thermal decomposition govern the process, depending on the droplet surface temperature. If the ambient temperature is larger than a specific value T^+ , thermal decomposition is very fast and vaporization dominates the total process time, whereas at lower ambient temperatures, the vaporization is slower, which causes a lower final droplet surface temperature, leading to considerably longer thermal decomposition, which dominates the total process time under that condition. The ambient temperature at which this reversed behavior occurs depends on initial INN loading of the particle and the relative velocity but is largely independent of the initial droplet size. These new results are very useful in choosing the process temperature, which is recommended to lie beyond the ambient air temperature of T^+ to assure that the total process time is kept short. The numerical results are parameterized for use in more complex simulations of FSP.



Citation: Narasu, P.; Gutheil, E. Modeling and Parameterization of the Evaporation and Thermal Decomposition of an Iron(III) Nitrate Nonahydrate/Ethanol Droplet for Flame Spray Pyrolysis. *Fluids* **2022**, *7*, 146. <https://doi.org/10.3390/fluids7050146>

Academic Editor: Mehrdad Massoudi

Received: 8 March 2022

Accepted: 19 April 2022

Published: 23 April 2022

Publisher's Note: MDPI stays neutral with regard to jurisdictional claims in published maps and institutional affiliations.



Copyright: © 2022 by the authors. Licensee MDPI, Basel, Switzerland. This article is an open access article distributed under the terms and conditions of the Creative Commons Attribution (CC BY) license (<https://creativecommons.org/licenses/by/4.0/>).

Keywords: precursor solution droplet; Iron(III) nitrate nonahydrate/ethanol; multicomponent droplet evaporation; thermal decomposition; total process time; parameterization

1. Introduction

Flame spray pyrolysis (FSP) is an efficient method to produce nanoparticles with special characteristics. A liquid precursor solution is injected, and after breakup and atomization, the droplets undergo heating, evaporation, and possible thermal decomposition, followed by gas-phase combustion and nanoparticle formation. Therefore, it is important to understand the dynamics of the precursor solution droplet, since it is significant in controlling the synthesis of nanoparticles [1].

Nanoparticles synthesized using FSP offers many advantages compared to those produced using gas-phase synthesis. For instance, the final particle properties may be controlled better in FSP, and a wider range of particles may be produced, such as alloys. Ding et al. [2] reported the production of thermally stable metal oxide-supported single-atom platinum catalysts using FSP; and they displayed excellent catalytic performance in CO oxidation, methane combustion, and methane partial oxidation reactions compared to those generated through the conventional methods. Gao et al. [3] employed FSP to synthesize catalysts with surface-supported isolated platinum atoms and concluded that the

performance and cost efficiency of catalysts were greatly improved. Deligiannakis et al. [4] used different FSP technology configurations for the controlled synthesis of nanocatalysts, which demonstrated considerable potential for clean and efficient hydrogen generation at near-ambient pressure and temperature. Yuan et al. [5] studied the one-step-synthesis of nanocatalysts by flame spray pyrolysis with varied copper loadings and precursor feeding rates with the aim of exploring the potential of cupric oxide in the catalytic combustion of carbon monoxide and methane, to help reduce pollution emissions. The influences of bifunctional copper components on titanium dioxide were experimentally and theoretically investigated via flame spray pyrolysis to optimize the photothermocatalytic efficiency for use in the elimination of air pollutants [6].

Meierhofer et al. [7] numerically investigated the evolution of zirconia primary and agglomerate nanoparticle diameters for a laboratory-scaled FSP reactor, and it was found that the numerical model estimated the nanoparticle diameters with 75% accuracy compared to experimental data. The synthesis of silica nanoparticles via FSP was also studied numerically [8], and it was found that the particle sizes and distributions predicted by the numerical model were in good agreement with the measurements. Madero et al. [9] computationally studied and compared the low-temperature flame spray pyrolysis (LT-FSP) to a flame-assisted spray pyrolysis system and concluded that the LT-FSP process provides a more uniform temperature distribution, which in turn achieves improved uniformity in the final product. Paulson et al. [10] employed machine learning techniques in order to optimize the FSP process, and observed a relative improvement of 18.9% after five experimental runs and an improvement of 25.5% after 15 runs.

Stodt et al. [1] studied the influence of precursor concentration on the evaporation process of INN in 2-ethylhexanoic acid and ethanol as the precursor solution system via detailed phase doppler anemometry (PDA) measurements in the *SpraySyn* burner [11]. Increased evaporation rates for the precursor-containing spray flames were found in comparison with the pure solvent spray flames. A new type of particle mass spectrometry, atmospheric pressure particle mass spectrometry (AP-PMS), was developed to detect the particle size distributions in spray flames at ambient pressure using the precursor solution system of INN in 2-ethylhexanoic acid and ethanol [12]. The direct comparison of the AP-PMS with the conventional measurement techniques showed that AP-PMS is more robust to higher particle number concentrations and pressures and is therefore, an attractive alternative for the investigation of particle growth processes in spray flames.

The phase-selective laser-induced breakdown spectroscopy (PS-LIBS) technique was applied to an external mixing spray flame reactor in order to study iron oxide particle formation, with the aim of differentiating between droplet-to-particle and gas-to-particle routes [13]. It was concluded that the transition of the unreacted precursor from droplet-to-particle phase is not detectable when applying PS-LIBS in the underlying dense spray flame. The production of iron oxide nanoparticles using two precursor formulations, namely, INN/ethanol and INN/ethanol in 2-ethylhexanoic acid, in a standardized *SpraySyn* burner system [11] was investigated experimentally [14]. It was concluded that gas-to-particle and droplet-to-particle pathways might coexist. The droplet-to-particle and gas-to-particle mechanisms are also mentioned in a review paper on the synthesis and processing of noble metal nanoparticles using ultrasonic spray pyrolysis [15].

Dasgupta et al. [16] simulated the processes of liquid spray breakup and evaporation, mixing, combustion, and particle formation/growth of silica nanoparticles in a simplified annular burner. The computed particle number density and volume fraction compared well with the CFD results presented by Rittler et al. [17]. The production of zirconium dioxide nanoparticles from a solution of zirconium *n*-propoxide in ethanol and propanol via FSP was numerically studied by Neto et al. [18]. The number of primary particles per agglomerate showed good agreement with experimental data obtained through transmission electron microscopy (TEM) with an accuracy of 90%.

Very few numerical studies have been performed where the droplet evaporation and the thermal decomposition processes were coupled. Widiyastuti et al. [19] performed a

numerical investigation of the spray pyrolysis of zirconia particle formation, and they concluded that the determination of the final particle size is influenced by both the evaporation and the decomposition processes. For temperatures lower than the decomposition temperature, the final particle size was found to be larger as compared to that for temperatures higher than the decomposition temperature. Moreover, an in situ modified spray pyrolysis system was used to study the purity of TiO₂ thin films deposited onto a glass substrate [20]. The mathematical model was used to calculate the final particle size by coupling the processes of atomization of the precursor solution, the droplet transport in ambient air, decomposition and evaporation of the precursor solution, and film growth. Narasu et al. [21] investigated the heating, evaporation, and thermal decomposition of INN/ethanol droplets numerically. Both the droplet-to-particle and the droplet into gas phase pathways were considered, and it was recommended to avoid the droplet-to-particle route, since it leads to the formation of large particles that are to be avoided in spray flame synthesis.

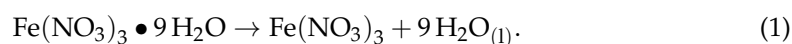
An earlier study of Narasu et al. [21] concerned the same system with initial INN mass fractions of 0.025. In that study, the focuses were the droplet-to-particle pathway, where no thermal decomposition occurs, and the effect of humid air on the process at higher ambient gas temperatures. In the following, initial mass loadings of up to 0.200 of the INN in the precursor solution are addressed. The impacts of vaporization and thermal decomposition times on the process characteristics are evaluated, and the numerical results are parametrized for use in more complex simulations of FSP.

2. Mathematical Model

The model includes the heating, evaporation, and thermal decomposition of an INN/ethanol droplet in hot convective air at atmospheric pressure. If the ambient temperature is below the thermal decomposition temperature T_{th} of the INN, the solvent and the water contained in the INN evaporate and a solid particle is left behind [21]. In the present study, the ambient temperature is assumed to be high enough for thermal decomposition to occur; and the influences of the initial precursor loading of INN on the heating, evaporation, and thermal decomposition characteristics are explored.

In the present model, it is assumed that the droplet is spherical all the time, the solubility of air in the liquid is negligible, mass diffusion due to temperature and pressure gradients is negligible, the gas phase is in a quasi-steady state, the droplet evaporates in a non-reacting inert environment, and the heat transfer due to radiation is negligible [22]. The activity coefficients of the INN/ethanol mixture are not available, and therefore, the precursor solution is treated as ideal. In order to assure that there is neither inner recirculation of the droplet nor flow separation in the wake of the droplet, low droplet Reynolds numbers up to about twenty are considered. The distillation-limit model and the rapid-mixing model are used to describe the droplet heating and evaporation, respectively, for low thermal and mass Peclet numbers [23]. Hence, no spatial resolution of the droplet interior is required. The formulation of the governing equations for the convective droplet heating and evaporation were chosen based on the study of Abramzon and Sirignano [24] with an extension for multicomponent droplets by Brenn et al. [22].

In the model, the INN is treated as the two components, iron(III) nitrate and water.



Therefore, the precursor solution droplet comprises the three components, iron(III) nitrate, water, and ethanol. If the droplet surface temperature exceeds the thermal decomposition temperature T_{th} of the INN, 403 K, the iron(III) nitrate thermally decomposes into iron(III) oxide, Fe₂O₃, and dinitrogen pentoxide, N₂O₅ [21]:



and the reaction rate is determined in terms of α

$$\alpha = 1 - \frac{Y_{\text{IN},t}}{Y_{\text{IN},0}}, \tag{3}$$

where $Y_{\text{IN},t}$ denotes the mass fraction of iron(III) nitrate at time t and $Y_{\text{IN},0}$ is the initial mass fraction of iron(III) nitrate. Thus, the entire liquid droplet is transferred into the gas phase.

The time derivative of α is given as [25]

$$\frac{d\alpha}{dt} = k_{\text{th}}(1 - \alpha)^n, \tag{4}$$

where the reaction order is $n = 2/3$ and k_{th} denotes the kinetic rate constant of the thermal decomposition

$$k_{\text{th}} = k_0 e^{-E/(RT)}. \tag{5}$$

The collision efficiency k_0 equals $2.60 \times 10^{44} \text{ s}^{-1}$, the activation energy E is 376.97 kJ/mol, R denotes the universal gas constant, and T denotes temperature.

In order to complete the model, the heating and evaporation of the ethanol



and the water



are described following the previous studies of Narasu et al. [21,23]. Note that the model allows for the condensation of the water.

The multicomponent droplet evaporation model is based on that of Brenn et al. [22] which is an advancement of that of Abramzon and Sirignano [24] for a single component droplet. The mass evaporation rate of the droplet yields [22]

$$\dot{m} = \sum_{i=1}^n 2\pi r_{d,i} \rho_f D_{f,i} \widetilde{\text{Sh}} \ln(1 + B_{M,i}), \tag{8}$$

where the Spalding mass transfer number $B_{M,i}$ for the individual components i is

$$B_{M,i} = \frac{Y_{s,i} - Y_{\infty,i}}{1 - Y_{s,i}}. \tag{9}$$

$Y_{s,i}$ is the mass fraction of component i at the droplet surface s , and $Y_{\infty,i}$ is that in the ambience. $D_{f,i}$ is the diffusion coefficient in the film f , and $\widetilde{\text{Sh}}$ is the modified Sherwood number that accounts for convective droplet evaporation [24].

The temperature T_s at the droplet surface, s , varies with time, t , as [22,24]

$$m c_{\text{pl}} \frac{dT_s}{dt} = 2\pi r_d \lambda_f \widetilde{\text{Nu}} \ln(1 + B_T) \frac{T_g - T_s}{B_T} - \sum_{i=1}^n \dot{m}_i L_{v,i}(T_s), \tag{10}$$

where the Spalding heat transfer number, B_T , is defined as [22,24]

$$B_T = (1 + \sum_{i=1}^n Y_i B_{M,i})^\phi - 1.0 \quad \text{with} \quad \phi = \frac{c_{\text{pl}} \widetilde{\text{Sh}}}{c_{\text{pf}} \widetilde{\text{Nu}} \text{Le}}. \tag{11}$$

The physical properties are provided by Narasu et al. [21] and the numerical solution procedure is that of Narasu et al. [21,23].

3. Results and Discussion

In the present study, the heating, evaporation, and thermal decomposition characteristics of a single droplet consisting of a precursor solution of INN and ethanol are

investigated with the aim of understanding the influences of the initial precursor loading in the solution on these processes. The initial precursor mass fractions of the droplet were chosen following the experiments of Schneider et al. [11] as 0.0125, 0.025, and 0.02, where the ratio of water to IN was 4:6. For these conditions, the distillation-limit and rapid-mixing models are valid for low thermal and mass Peclet numbers and the droplet breakup is not considered for low Weber numbers well below the critical Weber number [23]. Thermal decomposition occurs for ambient gas temperatures above the thermal decomposition temperature $T_{th} = 403$ K of the precursor, which is valid for the ambient gas temperatures of 800 and 1200 K under consideration.

3.1. Droplet Heating, Evaporation, and Thermal Decomposition

First, the principal physical processes are presented and discussed for several conditions.

Figure 1 displays the profiles of the temperature and the species mass fractions on the droplet surface with time for the precursor solution droplet with an initial droplet radius of $5 \mu\text{m}$, an initial mass fraction of INN of $Y_{INN,0} = 0.200$, and a relative velocity of 4 m/s at ambient temperatures of 1200 and 800 K; Figure 1a,b. The droplet surface temperature increases due to initial droplet heating, followed by the quasi-steady evaporation phase, during which the preferential evaporation of the higher volatile ethanol occurs and the water content inside the droplet increases. A major increase in droplet surface temperature occurs after about 0.3 and 0.6 ms for the higher and lower ambient gas temperatures, respectively, which results in the complete evaporation of ethanol and water. If the droplet surface temperature exceeds the thermal decomposition temperature of 403 K, the iron(III) nitrate transforms into the gas phase. Once the ethanol and water have completely evaporated, the thermal decomposition is the only process that is occurring in the system at constant temperature, which is determined by the droplet evaporation process. At the lower ambient temperature of 800 K, see Figure 1b, the overall process is prolonged due to the reduced heat transfer rate between the ambience and the droplet, which reduces the final droplet temperature by more than 30 K compared to the high-temperature ambience. Figure 1 shows that in the high-temperature ambience, the vaporization is the dominant process, whereas in the low-temperature ambience, the thermal decomposition governs the total process, leading to a considerable difference in the total process times. These are about 0.34 and 10.5 ms for the high-temperature ambience and low-temperature ambience for the conditions of Figure 1.

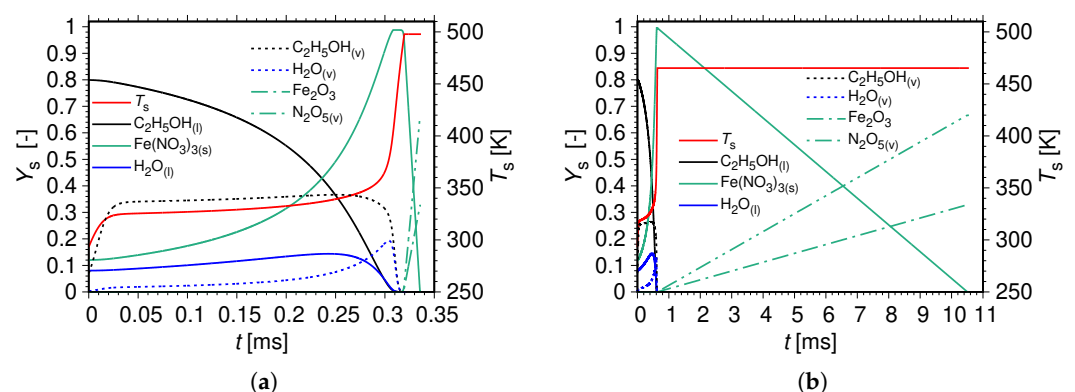


Figure 1. Species mass fractions and droplet surface temperatures versus time. Initial conditions: $r_{d,0} = 5 \mu\text{m}$, $T_{l,0} = 293.15 \text{ K}$, $p = 1 \text{ bar}$, $u_0 = 4 \text{ m/s}$, $Y_{C_2H_5OH,0} = 0.80$, $Y_{INN,0} = 0.200$. (a) $T = 1200 \text{ K}$. (b) $T = 800 \text{ K}$.

The vaporization process is further studied in Figure 2, which shows the heating and evaporation characteristics for an INN/ethanol droplet of initial droplet radius of $5 \mu\text{m}$ at relative velocities of 4 and 8 m/s for an initial INN mass fraction of 0.200 at ambient gas temperatures of 800 and 1200 K. Figure 2a displays the normalized droplet surface area

and Figure 2b the droplet surface temperature and the mass evaporation rates of ethanol and water versus time. Droplet heating causes initial droplet expansion, which is visible in the initial profile of $(d/d_0)^2$. This reflects the variable physical properties of the liquid, in particular that of the liquid density. After the unsteady droplet heating, quasi-steady droplet evaporation occurs, where the preferential evaporation of ethanol occurs due to its higher volatility compared to H_2O , followed by the evaporation of water and the thermal decomposition of iron(III) nitrate into the gas phase. During droplet expansion, there is an initial increase in the droplet surface temperature, see Figure 2b, which then remains almost constant during the quasi-steady vaporization period, following the classical behavior discussed also for single-droplet evaporation [26]. After the ethanol vaporization is almost complete, a second increase in the droplet surface temperature occurs and enhanced evaporation of water prevails as a consequence of its lower volatility compared to ethanol. At the higher relative velocity of 8 m/s, the droplet evaporation is enhanced due to stronger convection, and the final droplet surface temperature attained is reduced by approximately 10 K compared to the lower relative velocity. Even though this difference sounds small, it strongly affects the thermal decomposition process discussed next.

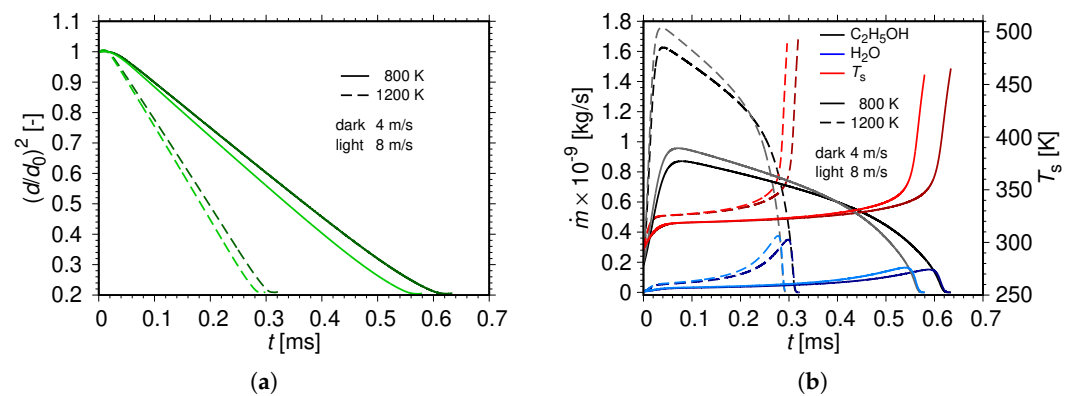


Figure 2. Initial conditions: $r_{d,0} = 5 \mu\text{m}$, $T_{l,0} = 293.15 \text{ K}$, $p = 1 \text{ bar}$, $u_0 = 4 \text{ m/s}$ and 8 m/s , $T_{g,0} = 800 \text{ K}$ and 1200 K , $Y_{C_2H_5OH,0} = 0.80$, $Y_{INN,0} = 0.200$. (a) Normalized droplet surface area with time. (b) Mass evaporation rate and droplet surface temperature with time.

Figure 3 shows the temperature dependence of the kinetic rate coefficient (solid line) and final droplet surface temperatures for various initial conditions (symbols). Figure 3b is a zoom of Figure 3a to better resolve the low-temperature region. At the higher ambient gas temperature of 1200 K (small symbols), the temperature attained at the droplet surface is higher due to the increased heat transfer rate between the ambience and the droplet compared to the lower ambient temperature (large symbols). Larger droplets undergo prolonged heating and evaporation, which results in lower final droplet surface temperatures, and thus, longer thermal decomposition times. At the higher relative velocity of 8 m/s (open symbols), the droplet evaporates faster, which leads to a lower final droplet surface temperature and thus prolongs the process of thermal decomposition compared to the lower ambient velocity (filled symbols). For the highest initial INN mass fraction of 0.200 (green), both the final droplet surface temperature and the reaction rate coefficient are smaller than those for the initial INN mass fractions of 0.0125 (blue) and 0.025 (red) since the evaporation is faster for the larger initial INN mass fractions, which leads to lower droplet surface temperatures, causing a prolongation of the thermal decomposition process. Depending on the final surface temperature attained by the droplet and the corresponding value of the kinetic rate coefficient, the overall process times vary for different initial conditions, which is discussed in the next subsection in more detail.

3.2. Process Time

Figures 4 and 5 show the total process times, τ_{tot} , for initial mass fractions of INN, $Y_{INN,0}$, of 0.0125, 0.025, and 0.200, at relative velocities of 4 m/s (part a) and 8 m/s (part b),

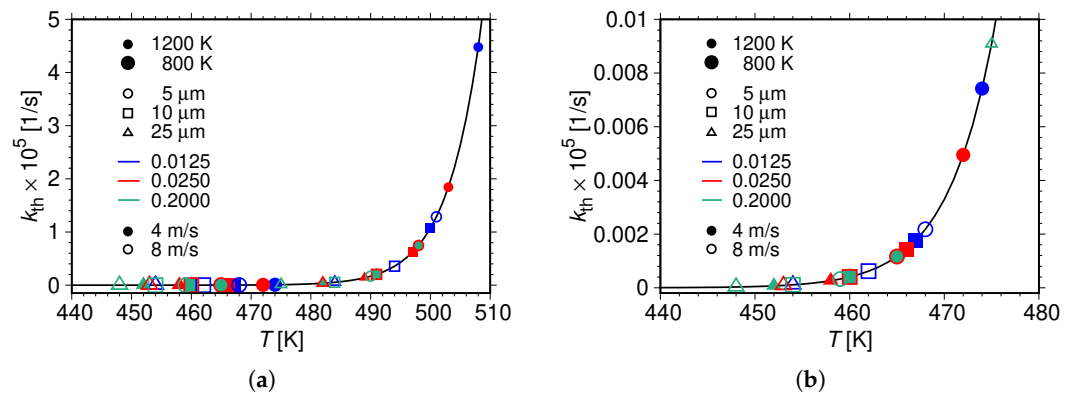


Figure 3. Rate coefficient of the thermal decomposition k_{th} versus temperature (solid line) and final droplet surface temperatures for various initial conditions (symbols). (a) k_{th} versus temperature. (b) Zoomed view.

for both ambient gas temperatures of 800 and 1200 K, respectively. The total process times increase with the initial droplet radius due to the prolonged droplet heating time and the lower final temperatures attained by the droplet, which results in longer thermal decomposition times. The process times are shorter at the higher ambient gas temperature of 1200 K due to the increased heat transfer rates between the ambience and the droplet surface, which result in higher droplet surface temperatures; see Figure 5. At the lower ambient temperature of 800 K, increasing the relative velocity from 4 m/s (see Figure 4a) to 8 m/s (see Figure 4b) enhances the vaporization process, which results in a reduced final droplet surface temperature, and thus prolongs the overall process time. However, at the higher ambient temperature of 1200 K, the overall process time is reduced at the higher relative velocity for initial INN mass fractions of 0.0125 and 0.025 (see Figure 5), because of the domination of the evaporation process. In the case of the higher mass fraction of INN of 0.200, owing to the lower temperatures attained by the droplet surface, see Figure 3, the thermal decomposition process is slowed down, which slightly increases the overall process time.

At the lower ambient temperature of 800 K, see Figure 4, the overall process time is prolonged for the higher initial INN mass fraction of 0.200, as compared to the initial INN mass fractions of 0.0125 and 0.025. At the higher ambient temperature of 1200 K, see Figure 5, this effect is reversed, which shows that an intermediate temperature, T^+ , must exist at which the reversal between these effects occurs. Since the total process time related to the droplet heating, evaporation, and thermal decomposition, plays a significant role in evaluating the global process time of the nanoparticle synthesis, the evaluation of the temperature T^+ would be helpful in deciding the selection of the conditions for FSP, which is discussed in Figure 6.

Figure 6a shows the total process times that consist of the droplet evaporation times (filled part of the columns) and the thermal decomposition times (shaded part of the columns), for an INN/ethanol droplet of initial radius 25 μm at relative velocity of 4 m/s for the initial INN mass fractions of 0.0125, 0.025, and 0.200, at different ambient gas temperatures, and Figure 6b displays the corresponding results for a relative velocity of 8 m/s.

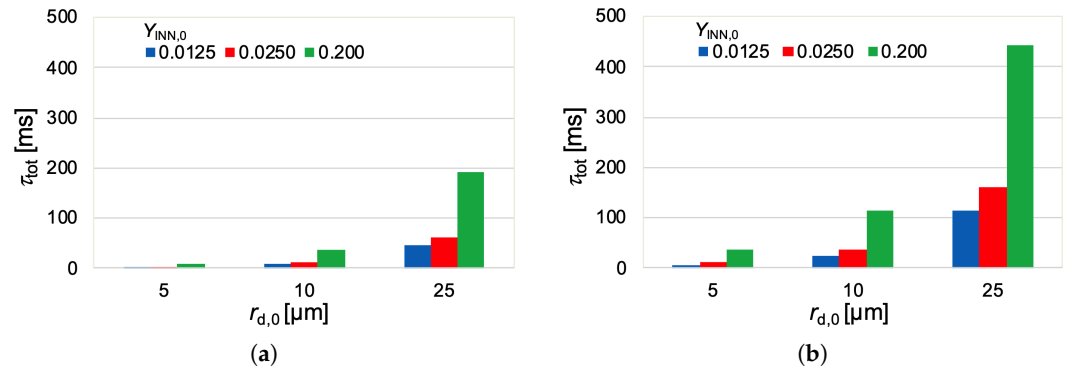


Figure 4. Total process times for different initial droplet radii and initial INN mass fractions of 0.0125, 0.025, and 0.200. Initial conditions: $T_{l,0} = 293.15$ K, $p = 1$ bar, $T_{g,0} = 800$ K. (a) $u_0 = 4$ m/s. (b) $u_0 = 8$ m/s.

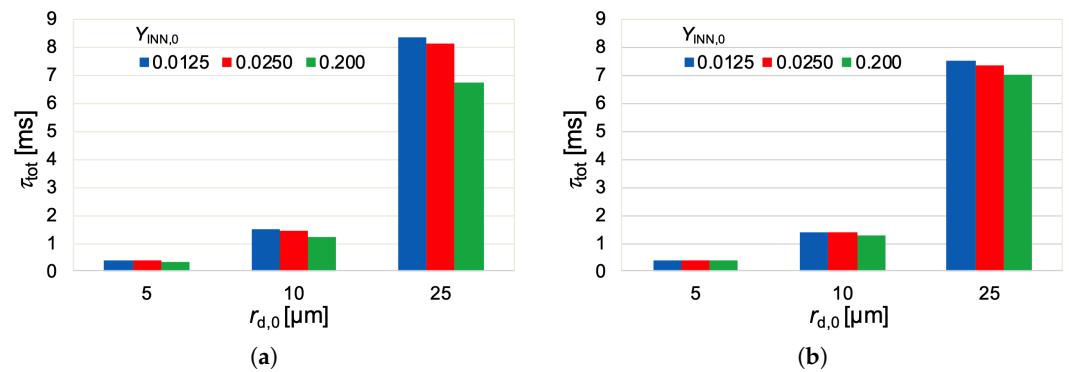


Figure 5. Total process times for different initial droplet radii and initial INN mass fractions of 0.0125, 0.025, and 0.200. Initial conditions: $T_{l,0} = 293.15$ K, $p = 1$ bar, $T_{g,0} = 1200$ K. (a) $u_0 = 4$ m/s. (b) $u_0 = 8$ m/s.

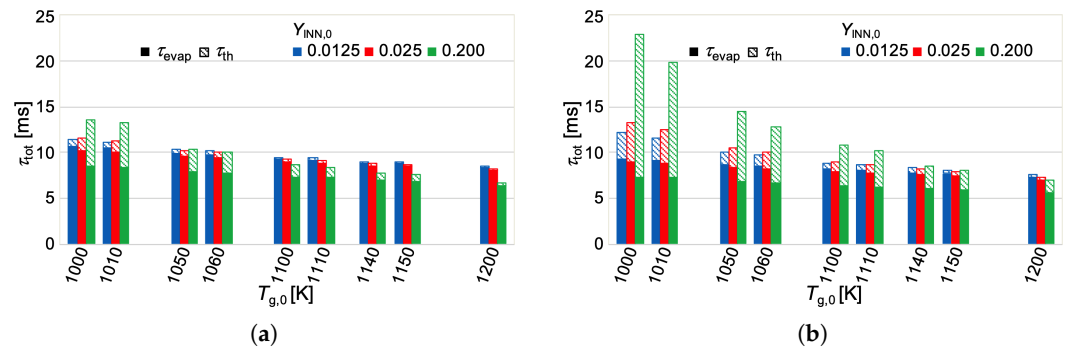


Figure 6. Contributions to the total process times for different initial INN mass fractions of 0.0125, 0.025, and 0.200. Initial conditions: $r_{d,0} = 25$ μm , $T_{l,0} = 293.15$ K, $p = 1$ bar. (a) $u_0 = 4$ m/s. (b) $u_0 = 8$ m/s.

A comparison of the total process times τ_{tot} for initial INN mass fractions of 0.025 and 0.200 at a relative velocity of 4 m/s displayed in Figure 6a shows that the total process time for the precursor solution droplet with the larger initial INN mass fraction is considerably longer at an ambient temperature of 1000 K, and the difference in τ_{tot} decreases with a higher ambient gas temperature due to the differences in evaporation and thermal decomposition times discussed above. At about $T^+ = 1060$ K, the behavior is reversed and τ_{tot} is longer for the lower initial mass fraction of the INN. It is interesting to note that the value of T^+ is independent of droplet size. The value of T^+ is approximately 1010 K for initial INN

mass fractions of 0.0125 and 0.025 and about 1050 K for INN mass fractions of 0.0125 and 0.200. Additionally, the evaporation process is faster at larger initial INN mass fractions, which leads to reduced final droplet surface temperature, and therefore, slows down the thermal decomposition process. At the higher relative velocity of 8 m/s, see Figure 6b, the droplet evaporation times are reduced due to the higher convection rate, and the thermal decomposition times are prolonged due to lower final droplet surface temperatures; see Figure 3b. Thus, at a relative velocity of 8 m/s, T^+ is higher than that at the lower relative velocity of 4 m/s for the different precursor loadings under investigation.

Figure 7 summarizes the variation of T^+ for the different INN mass fractions at relative velocities of 4 and 8 m/s. At both relative velocities, increasing the initial precursor mass fraction results in higher T^+ values, due to the faster evaporation process leading to lower final droplet surface temperatures and reaction rate coefficient values, which prolongs the thermal decomposition process more than that for the smaller initial INN mass fractions. The increase in T^+ for the higher relative velocity of 8 m/s compared to 4 m/s is approximately 100 K.

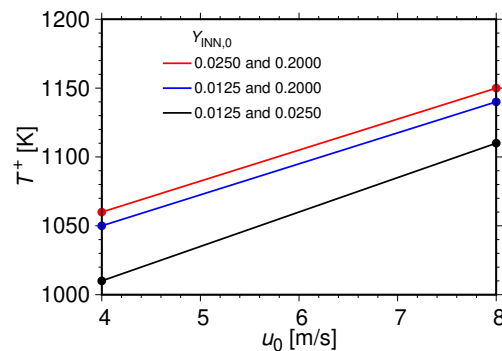


Figure 7. T^+ versus relative velocity for different initial INN mass fractions. Initial conditions: $T_{1,0} = 293.15$ K, $p = 1$ bar.

It is interesting to see that T^+ varies for different precursor mass fractions in the precursor solution and for different relative velocities, but it does not depend on the initial droplet radii, which were varied from 5 μm to 25 μm . It is recommended to choose an ambient process temperature higher than T^+ to ensure that the total process times are short.

The parametric dependence of vaporization and thermal decomposition characteristics may be used in more complex studies of FSP. For this purpose, the results of the present study are parametrized using polynomial fits in the next subsection.

3.3. Parameterization

The numerical results of the heating, vaporization, and thermal decomposition presented in the previous sections show some similarity, which will be analyzed and parameterized for use in more complex simulations of laminar or turbulent sprays. Results of an earlier study [21] will be included in the parameterization.

The procedure followed is similar to the parameterization of the heating and evaporation characteristics of the TTIP/*p*-xylene droplets [27], except for the process of thermal decomposition, which does not occur in that system. Therefore, in the present work, the parameterization of the thermal decomposition is discussed in detail. First, the parameters of interest are non-dimensionalized using the same reference values as in the earlier

study [27], except for the thermal decomposition time, t_{th} , which has to be added. Thus, the dimensionless quantities for parameterization are

$$\tau_{evap} = \frac{t}{t_{evap}} \quad (12)$$

$$\mathcal{T}_s = \frac{T_s}{T_{H_2O,b}} \quad (13)$$

$$\dot{\mathcal{M}}_i = \frac{\dot{m}_i}{m_0/t_{evap}}, \quad i = 1, 2 \quad (14)$$

$$\tau_{th} = \frac{t}{t_{th}} \quad (15)$$

In these equations, t_{evap} denotes the droplet evaporation time, $T_{H_2O,b}$ is the boiling temperature of the lower volatile component water, and m_0 is the initial droplet mass evaluated as $m_0 = 4/3\pi r_{d,0}^3 \rho_0$, where the density of the droplet is $\rho_0 = Y_{INN,0} \rho_{0,INN} + (1 - Y_{INN,0}) \rho_{0,C_2H_5OH}$. The initial densities $\rho_{0,i}$ are evaluated at the initial droplet temperature [28].

With these definitions, the dimensionless evaporation time is τ_{evap} , the dimensionless thermal decomposition time is τ_{th} , \mathcal{T}_s is the dimensionless droplet surface temperature, and $\dot{\mathcal{M}}_i$, $i = 1, 2$ denotes the normalized mass evaporation rates of ethanol and water. The normalized droplet surface area $(d/d_0)^2$ and the mass fraction of iron(III) nitrate Y_{IN} will also be parameterized, which are dimensionless per definition.

Figure 8a exemplarily displays profiles of the normalized mass evaporation rates and the normalized droplet surface temperatures for initial droplet radii from 5 to 25 μm and relative velocities of 4 and 8 m/s, for the initial mass fraction of INN of 0.025, at the initial ambient temperature of 1200 K. Moreover, the normalized droplet surface area plays a predominant role in droplet evaporation studies, which is presented in Figure 8b. For the normalized profiles, the arithmetic mean of the profiles for the different initial droplet radii were evaluated and added to the figures. It should be mentioned that the numerical time steps varied for every simulation, which changed the total number of time steps in the corresponding numerical simulation. Therefore, the number of time steps was adjusted to ten thousand in order to calculate the mean profile. At ambient temperatures above the thermal decomposition temperature, the thermal decomposition of iron(III) nitrate occurs. A detailed evaluation of the normalized results of the thermal decomposition characteristics reveals that the major influences are exerted through the ambient gas temperature, the initial INN mass fraction, and the relative velocity. The different initial droplet sizes show similarity and are represented through the dimensionless thermal decomposition times. Thus, two different graphs were obtained to represent the iron(III) nitrate mass fraction for initial INN mass fraction of 0.025 at an ambient temperature of 1200 K, which are presented in Figure 9a,b, for relative velocities of 4 and 8 m/s, respectively.

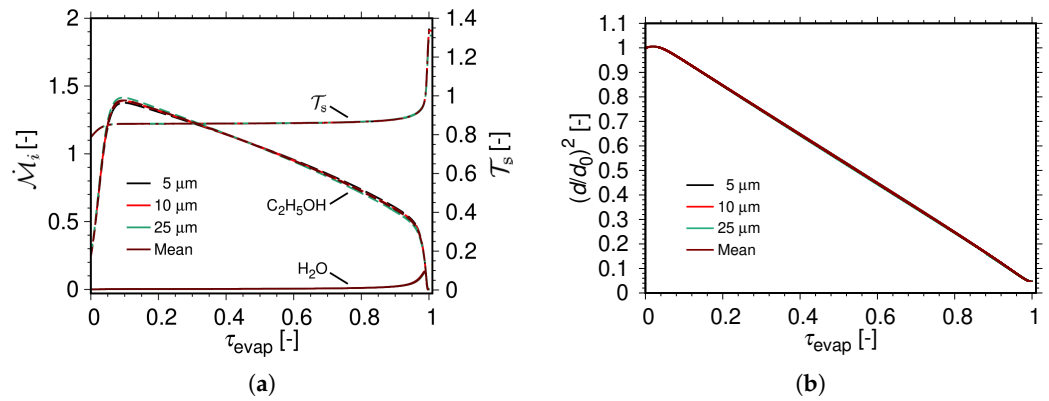


Figure 8. Normalized profiles with τ_{evap} for different initial droplet sizes. $T_{l,0} = 293.15$ K, $p = 1$ bar, $u_0 = 4$ m/s and 8 m/s, $T_{g,0} = 1200$ K, $Y_{\text{C}_2\text{H}_5\text{OH},0} = 0.975$, $Y_{\text{IN},0} = 0.025$. (a) Dimensionless mass evaporation rate and dimensionless droplet surface temperature versus normalized droplet evaporation time. (b) Normalized droplet surface area versus normalized droplet vaporization time.

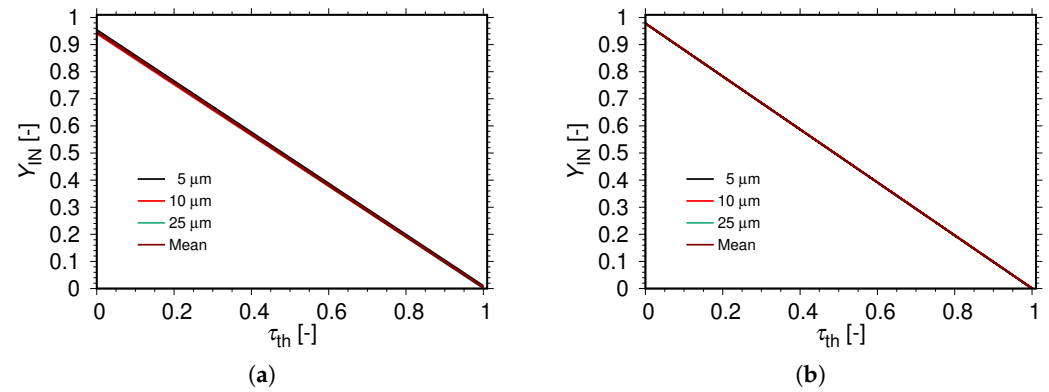


Figure 9. Profiles of the mass fraction of iron(III) nitrate with τ_{th} for different initial droplet sizes. $T_{l,0} = 293.15$ K, $p = 1$ bar, $T_{g,0} = 1200$ K, $Y_{\text{C}_2\text{H}_5\text{OH},0} = 0.975$, $Y_{\text{INN},0} = 0.025$. (a) $u_0 = 4$ m/s. (b) $u_0 = 8$ m/s.

For these averaged values, a polynomial fit is performed to parametrize the results.

3.4. Polynomial Fits

For the parameterization of the mean evaporation characteristics discussed in the previous section, a polynomial approach was chosen, which performs excellently to represent the numerical results [27]. A polynomial of degree 10 appears to be appropriate for all parameters, so that the approximation yields

$$\Gamma_{ik} = \sum_{j=0}^{10} a_{ikj} \tau_{\text{evap},ik}^j \begin{cases} k = 1, 2 & \text{for } \Gamma_i = T_s \\ k = 1, 2, 3 & \text{for } \Gamma_i = \dot{M}_{\text{C}_2\text{H}_5\text{OH}} \\ k = 1, 2, 3 & \text{for } \Gamma_i = \dot{M}_{\text{H}_2\text{O}} \\ k = 1 & \text{for } \Gamma_i = (d/d_0)^2 \end{cases} \quad (16)$$

where i represents the parameter being approximated, j stands for the degree of the polynomial, and k represents the number of polynomial fits required to describe the parameter. The normalized droplet surface temperature is described using two polynomial fits. The normalized mass evaporation rates of the components ethanol and water require three polynomials, and for the approximation of the normalized droplet surface area, a single polynomial is sufficient. Even though the approximation for the mass evaporation rates of ethanol and water requires three parts, the retrieval of this quantity may be performed with only two contributions, since the third part extends only over the last 1% of the normalized

droplet evaporation time (see also Figure 10), except for the case with the higher initial INN mass fraction of 0.200, which requires three contributions.

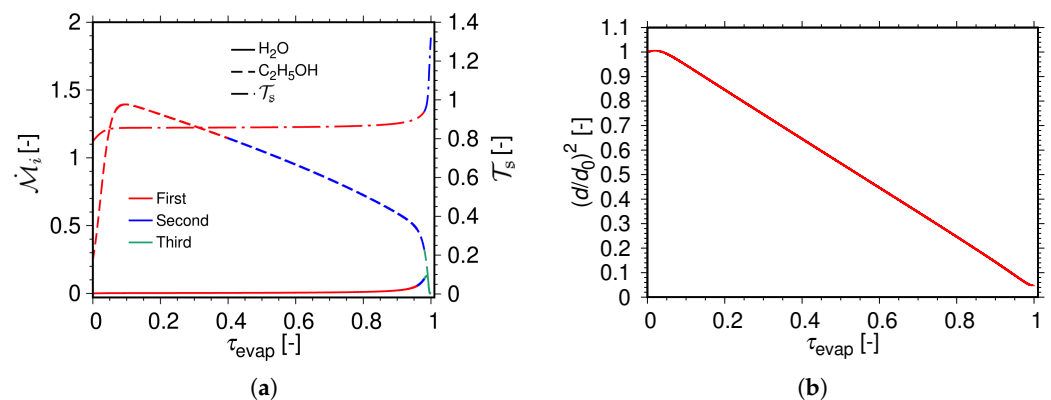


Figure 10. Fitted dimensionless profiles with normalized droplet evaporation time τ_{evap} . $T_{1,0} = 293.15$ K, $p = 1$ bar, $u_0 = 4$ m/s and 8 m/s, $T_{g,0} = 1200$ K, $Y_{\text{C}_2\text{H}_5\text{OH},0} = 0.975$, $Y_{\text{INN},0} = 0.025$. (a) Dimensionless mass evaporation rate and dimensionless droplet surface temperature with normalized vaporization time. (b) Normalized droplet surface area with normalized vaporization time.

Figure 10a displays the profiles of the dimensionless droplet surface temperature and the dimensionless mass evaporation rates of ethanol and water with evaporation time, and Figure 10b shows the normalized droplet surface area versus normalized evaporation time fitted via the polynomial equation for the average curves shown in Figure 8 for 1200 K. For the initial INN mass fractions of 0.0125, 0.025, and 0.200, two polynomial fits are required to capture the profile of the dimensionless droplet surface temperature, and three polynomial fits are required to describe the profile of the dimensionless mass evaporation rates of ethanol and water. The profile of the normalized droplet surface area is described with a single polynomial fit.

Figure 9 shows the profile of the mean of the mass fraction of iron(III) nitrate to be linear with thermal decomposition time so that providing the mean of the initial value of the iron(III) nitrate mass fraction is sufficient to describe the profile of the mass fraction of IN with t_{th} .

These polynomials may be used to retrieve the profiles of mass evaporation rates, droplet surface temperature, normalized droplet surface regression rate, and the mass fraction of iron(III) nitrate if the droplet evaporation times and the thermal decomposition times for each condition and the boiling point of water are provided. The data retrieval will be discussed next.

3.5. Tabulation and Retrieval of Simulation Results

Table 1 shows an example of the tabulation to retrieve the numerical results for an INN/ethanol droplet at ambient gas temperature of 1200 K for an initial INN mass fraction of 0.025. The organization of the data is similar to that described by Narasu et al. [27], except for the line in light blue, which gives two pairs of the relative velocity and the corresponding initial value of the iron(III) nitrate mass fraction; the relative velocities are in m/s. Additionally, each of the last three lines provide the initial droplet radius and two pairs of the droplet evaporation time and the thermal decomposition time for the relative velocities of 4 and 8 m/s; the droplet sizes are in μm and the process times in ms. Table A1 in Appendix A provides the full set of parameters for the initial INN mass fractions of 0.025 and 0.0125 at the initial ambient temperature of 400 K [21], and for the initial mass fractions of INN of 0.025, 0.0125, and 0.200 at the higher ambient temperatures of 800 and 1200 K. The second set of Table A1 is equal to the one presented in Table 1.

Table 1. Tabulated data of polynomial coefficients for normalized parameters as well as droplet evaporation and thermal decomposition times for different initial conditions at $T_{g,0} = 1200$ K and $Y_{INN,0} = 0.025$.

T_s	mdot_ethanol	mdot_water	$(d/d_0)^2$	0.025	1200
$7.867145821586 \times 10^{-01}$	$2.458546514703 \times 10^{+00}$	$-3.454578014776 \times 10^{+01}$	$2.558941751342 \times 10^{+02}$	$-1.119941643820 \times 10^{+03}$	$3.063310091836 \times 10^{+03}$
$-5.353792133168 \times 10^{+03}$	$5.941725000673 \times 10^{+03}$	$-4.019275839190 \times 10^{+03}$	$1.494058678680 \times 10^{+03}$	$-2.297048762642 \times 10^{+02}$	0.98
$3.007659971000 \times 10^{+07}$	$-6.120495257208 \times 10^{+07}$	$-9.902830762100 \times 10^{+06}$	$4.200275432824 \times 10^{+07}$	$4.198999581126 \times 10^{+07}$	$-5.113716178296 \times 10^{+05}$
$-4.347147946854 \times 10^{+07}$	$-4.342974843581 \times 10^{+07}$	$1.152668977259 \times 10^{+07}$	$6.702060944189 \times 10^{+07}$	$-3.409626488293 \times 10^{+07}$	1.00
$2.649827491167 \times 10^{-01}$	$6.467468055715 \times 10^{+00}$	$1.121608918537 \times 10^{+03}$	$-3.171074204381 \times 10^{+04}$	$4.068617331905 \times 10^{+05}$	$-3.044654355509 \times 10^{+06}$
$1.430867104877 \times 10^{+07}$	$-4.287019474526 \times 10^{+07}$	$7.959594503533 \times 10^{+07}$	$-8.353184950542 \times 10^{+07}$	$3.789437614192 \times 10^{+07}$	0.40
$-5.535923262976 \times 10^{+03}$	$8.969839635294 \times 10^{+04}$	$-6.472828661464 \times 10^{+05}$	$2.740187227611 \times 10^{+06}$	$-7.536843528899 \times 10^{+06}$	$1.407472429049 \times 10^{+07}$
$-1.807523129705 \times 10^{+07}$	$1.576513584004 \times 10^{+07}$	$-8.939005651413 \times 10^{+06}$	$2.976022992189 \times 10^{+06}$	$-4.418695467229 \times 10^{+05}$	0.98
$5.355407763709 \times 10^{-04}$	$1.217485456189 \times 10^{-03}$	$1.010741979324 \times 10^{+00}$	$-1.729839498434 \times 10^{+01}$	$1.318634067348 \times 10^{+02}$	$-5.604895163329 \times 10^{+02}$
$1.438672462980 \times 10^{+03}$	$-2.280482870988 \times 10^{+03}$	$2.183751108664 \times 10^{+03}$	$-1.158085428036 \times 10^{+03}$	$2.611880933761 \times 10^{+02}$	0.96
$-1.24420427367 \times 10^{+08}$	$4.102654147558 \times 10^{+08}$	$-2.569441893389 \times 10^{+08}$	$-3.234340385848 \times 10^{+08}$	$1.143042667218 \times 10^{+08}$	$3.802439643503 \times 10^{+08}$
$1.135102030104 \times 10^{+08}$	$-3.621309429414 \times 10^{+08}$	$-2.947956283717 \times 10^{+08}$	$5.065214628272 \times 10^{+08}$	$-1.630984700822 \times 10^{+08}$	0.98
$1.000238817552 \times 10^{+00}$	$6.485587657779 \times 10^{-01}$	$-2.281399335789 \times 10^{+01}$	$1.648888218078 \times 10^{+02}$	$-7.030976392018 \times 10^{+02}$	$1.873519086859 \times 10^{+03}$
$-3.191143274565 \times 10^{+03}$	$3.454879972907 \times 10^{+03}$	$-2.284257683482 \times 10^{+03}$	$8.330356340793 \times 10^{+02}$	$-1.266164668291 \times 10^{+02}$	1.00
4	$9.471258445809 \times 10^{-01}$	8	$9.781422439604 \times 10^{-01}$		
5	$0.388001000000 \times 10^{+00}$	$0.363501000000 \times 10^{+00}$	$0.006200000000 \times 10^{+00}$	$0.015900000000 \times 10^{+00}$	
10	$1.454101000000 \times 10^{+00}$	$1.328901000000 \times 10^{+00}$	$0.014200000000 \times 10^{+00}$	$0.059300000000 \times 10^{+00}$	
25	$8.020566000000 \times 10^{+00}$	$7.058666000000 \times 10^{+00}$	$0.085000000000 \times 10^{+00}$	$0.304000000000 \times 10^{+00}$	

The retrieval of the original simulation results is demonstrated for an INN/ethanol droplet of initial radius 5 μm at an ambient gas temperature of 1200 K for an initial INN mass fraction of 0.025 at a relative velocity of 4 m/s. At first, the polynomial fits in Equation (16) for the corresponding conditions were used to compute the mean values of the normalized parameter, with a normalized time step of 0.02. With respect to the mass evaporation rates of ethanol and water, the third range of polynomial fit is valid within 0.99 to 1.0 of the normalized evaporation time. During this period, the ethanol and water almost completely evaporated. Hence, the third polynomial fit corresponding to the normalized mass evaporation rates of ethanol and water was neglected, and their value was taken as zero for the final time step. By making use of the droplet evaporation time and the thermal decomposition time corresponding to the condition under investigation, the value of the boiling point of water, and the equations for the normalized parameters, the profile of the droplet surface temperature, the mass evaporation rates of the two components, the droplet surface area, and the mass fraction of iron(III) nitrate with time were calculated and are presented in Figures 11 and 12. The solid lines display the results obtained from the simulation, and the dashed lines depict the curves calculated from the polynomial fits.

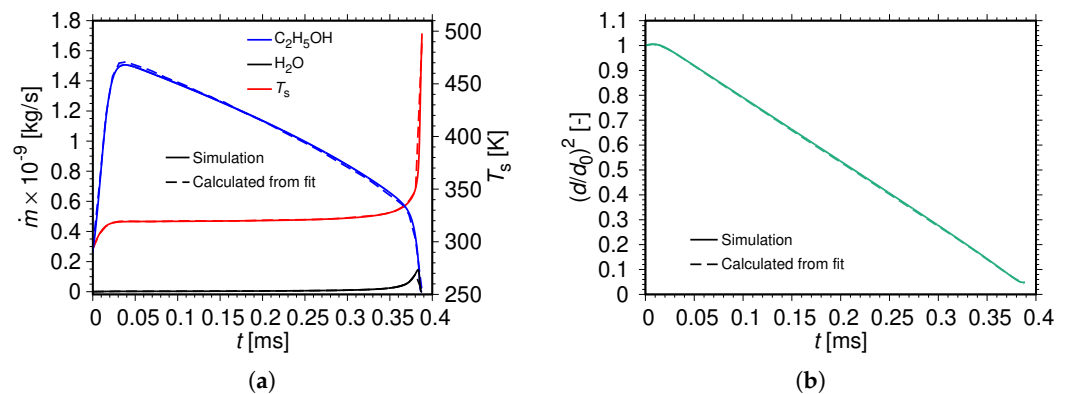


Figure 11. Initial conditions: $r_{d,0} = 5 \mu\text{m}$, $T_{l,0} = 293.15$ K, $p = 1$ bar, $u_0 = 4$ m/s, $T_{g,0} = 1200$ K, $Y_{C_2H_5OH,0} = 0.975$, $Y_{INN,0} = 0.025$. (a) Mass evaporation rate and droplet surface temperature with time. (b) Normalized droplet surface area with time.

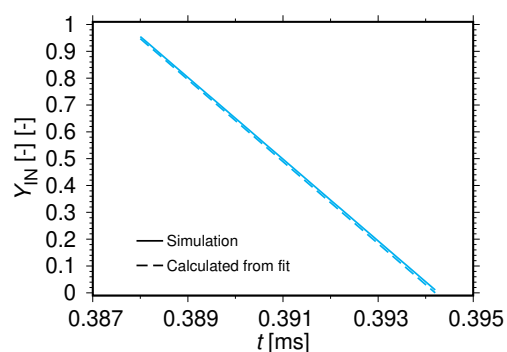


Figure 12. Mass fraction of iron(III) nitrate with time. Initial conditions: $r_{d,0} = 5 \mu\text{m}$, $T_{1,0} = 293.15 \text{ K}$, $p = 1 \text{ bar}$, $u_0 = 4 \text{ m/s}$, $T_{g,0} = 1200 \text{ K}$, $Y_{\text{C}_2\text{H}_5\text{OH},0} = 0.975$, $Y_{\text{INN},0} = 0.025$.

It is recommended to use the values of droplet evaporation time and thermal decomposition time with at least four decimal places and coefficients of the polynomial fits with a minimum of twelve decimal places to ensure precise computation of the profiles of the parameters. For each of the parameters considered, the overall error between the profiles computed using the polynomial fits and the simulation results was below 1.5%.

During complex simulations of FSP, it is not possible to incorporate a detailed simulation of the multicomponent droplet evaporation and thermal decomposition because of the limitations of computational resources. In such scenarios, the present parameterization is very useful.

4. Summary and Conclusions

A numerical parameter study of the heating, evaporation, and thermal decomposition of single INN/ethanol precursor droplets has been performed for use in more complex simulations of nanoparticle synthesis in spray flames.

INN/ethanol precursor solution droplets in hot convective air are investigated for a droplet size range of $5 \mu\text{m}$ to $25 \mu\text{m}$. The droplet heating and evaporation dominate the overall process at an ambient gas temperature of 1200 K , whereas the thermal decomposition is dominant at the lower ambient temperature of 800 K . This is due to the differences in the final droplet surface temperatures attained during the droplet evaporation process, which are considerably lower for the lower ambient gas temperature, which slows down the temperature-dependent thermal decomposition. Increasing the precursor mass fraction for fixed initial droplet size results in faster evaporation of the precursor solution droplet, and a lower final temperature is reached at the droplet surface, thereby prolonging the thermal decomposition time.

At the higher ambient temperature of 1200 K , increasing the precursor mass fraction in the range of 0.0125 and 0.2000 for fixed initial droplet size results in a reduction in the overall process time. However, this effect is reversed at a lower ambient temperature of 800 K . For two specific precursor loadings, this behavior occurs at the same value of the ambient gas temperature, T^+ , irrespective of the choice of the value of the initial droplet radii of 5 to $25 \mu\text{m}$ considered in the present study. Increasing the relative velocity from 4 to 8 m/s increases T^+ by approximately 100 K . Since the droplet evaporation and thermal decomposition times contribute to the total process times during the synthesis of nanoparticles, the knowledge of T^+ is helpful in selecting the conditions for FSP. It is recommended to select an ambient gas temperature higher than T^+ to keep the overall process time short.

The profiles of the droplet surface temperature, the mass evaporation rates of ethanol and water, the normalized droplet surface area, and the mass fraction of iron(III) nitrate were parametrized and described using polynomial fits. The present results may be used in more complex simulations where INN/ethanol precursor solutions are used for the synthesis of nanoparticles in FSP.

Author Contributions: P.N.: formal analysis, investigation, original draft preparation, review and editing. E.G.: conceptualization, methodology, resources, review and editing, supervision, project administration, funding acquisition. All authors have read and agreed to the published version of the manuscript.

Funding: Funding by the Deutsche Forschungsgemeinschaft (DFG, German Research Foundation) through SPP 1980–Projektnummer 374463455 is gratefully acknowledged.

Institutional Review Board Statement: Not applicable.

Informed Consent Statement: Not applicable.

Data Availability Statement: Available upon request.

Conflicts of Interest: The authors declare no conflict of interest.

Appendix A. Polynomial Coefficients, Droplet Evaporation, and Thermal Decomposition Times

Table [A1](#) provides all data for the retrieval of the heating, evaporation, and thermal decomposition characteristics.

Table A1. Polynomial coefficients.

T_s	mdot_ethanol	mdot_water	$(d/d_0)^2$	0.025	800
$7.867359690591 \times 10^{-01}$	$1.747616394195 \times 10^{+00}$	$-2.312503267622 \times 10^{+01}$	$1.615854300254 \times 10^{+02}$	$-6.634820152282 \times 10^{+02}$	$1.681763960325 \times 10^{+03}$
$-2.664277105596 \times 10^{+03}$	$2.576599396956 \times 10^{+03}$	$-1.405152642616 \times 10^{+03}$	$3.470305154648 \times 10^{+02}$	$-1.251614391388 \times 10^{+01}$	0.98
$1.321788785208 \times 10^{+07}$	$-2.698997242649 \times 10^{+07}$	$-4.289653155658 \times 10^{+06}$	$1.860013374498 \times 10^{+07}$	$1.851624158345 \times 10^{+07}$	$-3.214339097653 \times 10^{+05}$
$-1.929862335301 \times 10^{+07}$	$-1.919975663692 \times 10^{+07}$	$5.198552438105 \times 10^{+06}$	$2.975334052134 \times 10^{+07}$	$-1.518691541518 \times 10^{+07}$	1.00
$4.049928500265 \times 10^{-01}$	$1.402068766769 \times 10^{+01}$	$5.590321897474 \times 10^{+02}$	$-1.837923088876 \times 10^{+04}$	$2.417769740843 \times 10^{+05}$	$-1.817936365063 \times 10^{+06}$
$8.540484953760 \times 10^{+06}$	$-2.554575902726 \times 10^{+07}$	$4.734574245018 \times 10^{+07}$	$-4.961016526826 \times 10^{+07}$	$2.247808444881 \times 10^{+07}$	0.40
$-2.042865679835 \times 10^{+03}$	$3.324992865363 \times 10^{+04}$	$-2.409797491151 \times 10^{+05}$	$1.024856616974 \times 10^{+06}$	$-2.832688925475 \times 10^{+06}$	$5.317552375646 \times 10^{+06}$
$-6.866898241760 \times 10^{+06}$	$6.024603170622 \times 10^{+06}$	$-3.437402257253 \times 10^{+06}$	$1.151999845723 \times 10^{+06}$	$-1.722499714524 \times 10^{+05}$	0.98
$7.004499984111 \times 10^{-04}$	$7.320841215824 \times 10^{-03}$	$6.985636575392 \times 10^{-01}$	$-1.264700266326 \times 10^{+01}$	$9.813146413021 \times 10^{+01}$	$-4.211053619002 \times 10^{+02}$
$1.088454183635 \times 10^{+03}$	$-1.735749149109 \times 10^{+03}$	$1.671629805079 \times 10^{+03}$	$-8.915648471500 \times 10^{+02}$	$2.022706210720 \times 10^{+02}$	0.96
$-9.382191114812 \times 10^{+07}$	$3.094568746672 \times 10^{+08}$	$-1.939972472475 \times 10^{+08}$	$-2.439799160664 \times 10^{+08}$	$8.64560620347 \times 10^{+07}$	$2.870304398015 \times 10^{+08}$
$8.550078823384 \times 10^{+07}$	$-2.735465696351 \times 10^{+08}$	$-2.224800808429 \times 10^{+08}$	$3.826532228996 \times 10^{+08}$	$-1.232716072344 \times 10^{+08}$	0.98
$1.000289904692 \times 10^{+00}$	$2.936087644462 \times 10^{-01}$	$-1.773320982005 \times 10^{+01}$	$1.252323804627 \times 10^{+02}$	$-5.234968870397 \times 10^{+02}$	$1.369006095653 \times 10^{+03}$
$-2.284585819393 \times 10^{+03}$	$2.411780969212 \times 10^{+03}$	$-1.540582055775 \times 10^{+03}$	$5.335670240812 \times 10^{+02}$	$-7.443802056633 \times 10^{+01}$	1.00
4	$9.953996022681 \times 10^{-01}$	8	$9.959139590121 \times 10^{-01}$		
5	$0.714201000000 \times 10^{+00}$	$0.659601000000 \times 10^{+00}$	$2.470800000000 \times 10^{+00}$	$10.270399000000 \times 10^{+00}$	
10	$2.638701000000 \times 10^{+00}$	$2.371301000000 \times 10^{+00}$	$3.761000000000 \times 10^{+00}$	$8.705399000000 \times 10^{+00}$	
25	$14.230370000000 \times 10^{+00}$	$12.304500000000 \times 10^{+00}$	$46.286800000000 \times 10^{+00}$	$145.308700000000 \times 10^{+00}$	
T_s	mdot_ethanol	mdot_water	$(d/d_0)^2$	0.025	1200
$7.867145821586 \times 10^{-01}$	$2.458546514703 \times 10^{+00}$	$-3.454578014776 \times 10^{+01}$	$2.558941751342 \times 10^{+02}$	$-1.119941643820 \times 10^{+03}$	$3.063310091836 \times 10^{+03}$
$-5.353792133168 \times 10^{+03}$	$5.941725000673 \times 10^{+03}$	$-4.019275839190 \times 10^{+03}$	$1.494058678680 \times 10^{+07}$	$-2.297048762642 \times 10^{+02}$	0.98
$3.007659971000 \times 10^{+07}$	$-6.120495257208 \times 10^{+07}$	$-9.902830762100 \times 10^{+06}$	$4.200275432824 \times 10^{+07}$	$1.998999581126 \times 10^{+07}$	$-5.113716178296 \times 10^{+05}$
$-4.347147946854 \times 10^{+07}$	$-4.342974843581 \times 10^{+07}$	$1.152668972259 \times 10^{+07}$	$6.702060944189 \times 10^{+07}$	$-3.409626488293 \times 10^{+07}$	1.00
$2.649827491167 \times 10^{-01}$	$6.467468055715 \times 10^{+00}$	$1.121608918537 \times 10^{+03}$	$-3.171074204381 \times 10^{+04}$	$4.068617331905 \times 10^{+05}$	$-3.044654355509 \times 10^{+06}$
$1.430867104877 \times 10^{+07}$	$-4.287019474526 \times 10^{+07}$	$7.959594503533 \times 10^{+07}$	$-8.353184950542 \times 10^{+07}$	$3.789437614192 \times 10^{+07}$	0.40
$-5.535923262976 \times 10^{+03}$	$8.969839635294 \times 10^{+04}$	$-6.472828661464 \times 10^{+05}$	$2.740187227611 \times 10^{+06}$	$-7.536843528899 \times 10^{+06}$	$1.407472429049 \times 10^{+07}$
$-1.807523129705 \times 10^{+07}$	$1.576513584004 \times 10^{+07}$	$-8.939005651413 \times 10^{+06}$	$2.976022992189 \times 10^{+06}$	$-4.418695467229 \times 10^{+05}$	0.98
$5.355407763709 \times 10^{-04}$	$1.217485456189 \times 10^{-03}$	$1.010741979324 \times 10^{+00}$	$-1.729839498434 \times 10^{+01}$	$1.318634067348 \times 10^{+02}$	$-5.604895163329 \times 10^{+02}$
$1.438672462980 \times 10^{+03}$	$-2.280482870988 \times 10^{+03}$	$2.183751108664 \times 10^{+03}$	$-1.158085428036 \times 10^{+03}$	$2.611880933761 \times 10^{+02}$	0.96
$-1.244420427367 \times 10^{+08}$	$4.102654147558 \times 10^{+08}$	$-2.569441893389 \times 10^{+08}$	$-3.234340385848 \times 10^{+08}$	$1.143042667218 \times 10^{+08}$	$3.802439643503 \times 10^{+08}$
$1.135102030104 \times 10^{+08}$	$-3.621309429414 \times 10^{+08}$	$-2.947956283717 \times 10^{+08}$	$5.065214628272 \times 10^{+08}$	$-1.630984700822 \times 10^{+08}$	0.98
$1.000238817552 \times 10^{+00}$	$6.485587567779 \times 10^{-01}$	$-2.281399335789 \times 10^{+01}$	$1.648888218078 \times 10^{+02}$	$-7.030976392018 \times 10^{+02}$	$1.873519086859 \times 10^{+03}$
$-3.191143274565 \times 10^{+03}$	$3.454879972907 \times 10^{+03}$	$-2.284257683482 \times 10^{+03}$	$8.330356340793 \times 10^{+02}$	$-1.266164668291 \times 10^{+02}$	1.00
4	$9.471258445809 \times 10^{-01}$	8	$9.781422439604 \times 10^{-01}$		
5	$0.388001000000 \times 10^{+00}$	$0.363501000000 \times 10^{+00}$	$0.006200000000 \times 10^{+00}$	$0.015900000000 \times 10^{+00}$	
10	$1.454101000000 \times 10^{+00}$	$1.328901000000 \times 10^{+00}$	$0.014200000000 \times 10^{+00}$	$0.059300000000 \times 10^{+00}$	
25	$8.020566000000 \times 10^{+00}$	$7.058666000000 \times 10^{+00}$	$0.085000000000 \times 10^{+00}$	$0.304000000000 \times 10^{+00}$	
T_s	mdot_ethanol	mdot_water	$(d/d_0)^2$	0.025	400
$7.863412201930 \times 10^{-01}$	$-5.596710255187 \times 10^{-03}$	$7.798673182253 \times 10^{-01}$	$-1.297379984485 \times 10^{+01}$	$9.975999440013 \times 10^{+01}$	$-4.294562346831 \times 10^{+02}$
$1.115593134769 \times 10^{+03}$	$-1.786913375918 \times 10^{+03}$	$1.726649103043 \times 10^{+03}$	$-9.229611868066 \times 10^{+02}$	$2.096557240873 \times 10^{+02}$	0.96
$4.327485463200 \times 10^{+07}$	$-1.420829733550 \times 10^{+08}$	$8.878482597668 \times 10^{+07}$	$1.107328831258 \times 10^{+08}$	$-3.931565613548 \times 10^{+07}$	$-1.289473838013 \times 10^{+05}$
$-3.788109751754 \times 10^{+07}$	$1.216241556876 \times 10^{+08}$	$9.787607058016 \times 10^{+07}$	$-1.678799308370 \times 10^{+08}$	$5.381425268914 \times 10^{+07}$	1.00
$1.531480084513 \times 10^{+00}$	$4.785051289419 \times 10^{-01}$	$-2.248358016042 \times 10^{+01}$	$-1.895204961594 \times 10^{+02}$	$-9.673053825490 \times 10^{+02}$	$3.126326310656 \times 10^{+03}$
$-6.552662882402 \times 10^{+03}$	$8.876379844265 \times 10^{+03}$	$-7.497755187025 \times 10^{+03}$	$3.590661591465 \times 10^{+03}$	$-7.448170524673 \times 10^{+02}$	0.96
$-1.627867255534 \times 10^{+06}$	$5.723643530561 \times 10^{+06}$	$-4.077842548455 \times 10^{+06}$	$-4.510212130202 \times 10^{+06}$	$2.209964176216 \times 10^{+06}$	$5.765295109952 \times 10^{+06}$
$1.219165401094 \times 10^{+06}$	$-5.923272862578 \times 10^{+06}$	$-4.250988691443 \times 10^{+06}$	$8.268980803539 \times 10^{+06}$	$-2.796865533756 \times 10^{+06}$	0.98
$2.007980299564 \times 10^{-03}$	$-2.849737850328 \times 10^{-03}$	$2.110074500648 \times 10^{-01}$	$-3.058608732265 \times 10^{+00}$	$2.311805681849 \times 10^{+01}$	$-1.011391492653 \times 10^{+02}$
$2.711026039274 \times 10^{+02}$	$-4.516878664993 \times 10^{+02}$	$4.563096027000 \times 10^{+02}$	$-2.559639457377 \times 10^{+02}$	$6.122272040275 \times 10^{+01}$	0.96
$-3.434773944602 \times 10^{+07}$	$1.128861736657 \times 10^{+08}$	$-7.069061556954 \times 10^{+07}$	$-8.799281912150 \times 10^{+07}$	$3.142472975938 \times 10^{+07}$	$1.026209107149 \times 10^{+08}$
$3.000416840101 \times 10^{+07}$	$-9.693919852327 \times 10^{+07}$	$-7.785546174139 \times 10^{+07}$	$1.338354041063 \times 10^{+08}$	$-4.294555224574 \times 10^{+07}$	0.98
$1.000021336987 \times 10^{+00}$	$-1.050836018406 \times 10^{+00}$	$6.470737723956 \times 10^{-02}$	$-2.486456955154 \times 10^{+00}$	$2.384077785236 \times 10^{+01}$	$-1.104888213757 \times 10^{+02}$
$2.952114185993 \times 10^{+02}$	$-4.770194050724 \times 10^{+02}$	$4.608457970917 \times 10^{+02}$	$-2.453507475778 \times 10^{+02}$	$5.547886968102 \times 10^{+01}$	1.00
1	$0.157760100000 \times 10^{+00}$	$0.149597000000 \times 10^{+00}$			
2	$0.598526300000 \times 10^{+00}$	$0.556698900000 \times 10^{+00}$			
5	$3.421601000000 \times 10^{+00}$	$3.077001000000 \times 10^{+00}$			
T_s	mdot_ethanol	mdot_water	$(d/d_0)^2$	0.0125	800
$7.868617734492 \times 10^{-01}$	$1.758780317274 \times 10^{+00}$	$-2.393496998021 \times 10^{+01}$	$1.723320694844 \times 10^{+02}$	$-7.331690010150 \times 10^{+02}$	$1.943564131765 \times 10^{+03}$
$-3.271580345032 \times 10^{+03}$	$3.459558997750 \times 10^{+03}$	$-2.188901128876 \times 10^{+03}$	$7.353653211725 \times 10^{+02}$	$-9.485217956632 \times 10^{+01}$	0.98
$7.047907477452 \times 10^{+07}$	$-1.426166002927 \times 10^{+08}$	$-2.375181013842 \times 10^{+07}$	$9.719035423592 \times 10^{+07}$	$9.784591995507 \times 10^{+07}$	$-3.517901502225 \times 10^{+05}$
$-1.001680200667 \times 10^{+08}$	$-1.007750366360 \times 10^{+08}$	$2.584768640802 \times 10^{+07}$	$1.544258868402 \times 10^{+08}$	$-7.812566367591 \times 10^{+07}$	1.00
$4.126990862295 \times 10^{-01}$	$1.587859279807 \times 10^{+01}$	$5.433748013738 \times 10^{+02}$	$-1.895347351970 \times 10^{+04}$	$2.557331123657 \times 10^{+05}$	$-1.957513503559 \times 10^{+06}$
$9.326856980810 \times 10^{+06}$	$-2.822461589634 \times 10^{+07}$	$5.282737130968 \times 10^{+07}$	$-5.582212640641 \times 10^{+07}$	$2.54792913217 \times 10^{+07}$	0.40
$-3.140067363750 \times 10^{+03}$	$5.086094640437 \times 10^{+04}$	$-3.668092331303 \times 10^{+05}$	$1.551877336283 \times 10^{+06}$	$-4.265667520147 \times 10^{+06}$	$7.960630714181 \times 10^{+06}$
$-1.021626005120 \times 10^{+07}$	$8.904253978322 \times 10^{+06}$	$-5.045138362832 \times 10^{+06}$	$1.678408981624 \times 10^{+06}$	$-2.490167132284 \times 10^{+05}$	0.98
$3.488613880948 \times 10^{-04}$	$-4.106384001527 \times 10^{-03}$	$5.049113808918 \times 10^{-01}$	$-8.083100839664 \times 10^{+00}$	$6.051457177350 \times 10^{+01}$	$-2.555678218551 \times 10^{+02}$
$6.544282754021 \times 10^{+02}$	$-1.036614480031 \times 10^{+03}$	$9.927020829343 \times 10^{+02}$	$-5.266801462965 \times 10^{+02}$	$1.188617578409 \times 10^{+02}$	0.96
$-1.817677000307 \times 10^{+07}$	$5.992416850793 \times 10^{+07}$	$-3.752691593343 \times 10^{+07}$	$-4.724149621272 \times 10^{+07}$	$1.669139818970 \times 10^{+07}$	$5.553594621465 \times 10^{+07}$
$1.658230407641 \times 10^{+07}$	$-5.288642034695 \times 10^{+07}$	$-4.305706005033 \times 10^{+07}$	$7.397204317396 \times 10^{+07}$	$-2.381719756600 \times 10^{+07}$	

Table A1. Cont.

	T_s	mdot_ethanol	mdot_water	$(d/d_0)^2$	0.0125	1200
	7.871035810002 × 10 ⁻⁰¹	2.479094384565 × 10 ⁺⁰⁰	-3.576394894957 × 10 ⁺⁰¹	2.715466214038 × 10 ⁺⁰²	-1.219165305031 × 10 ⁺⁰³	3.429086238996 × 10 ⁺⁰³
	-6.188502974257 × 10 ⁺⁰³	7.138163354789 × 10 ⁺⁰³	-5.068241127543 × 10 ⁺⁰³	2.008263136505 × 10 ⁺⁰³	-3.377133696950 × 10 ⁺⁰²	0.98
	1.012954373676 × 10 ⁺⁰⁸	-2.048628275244 × 10 ⁺⁰⁸	-3.421278542091 × 10 ⁺⁰⁷	1.395148551837 × 10 ⁺⁰⁸	1.405520582274 × 10 ⁺⁰⁸	-3.882704757331 × 10 ⁺⁰⁵
	-1.437301465432 × 10 ⁺⁰⁸	-1.447002895719 × 10 ⁺⁰⁸	3.698812745779 × 10 ⁺⁰⁷	2.215835426858 × 10 ⁺⁰⁸	-1.120397000414 × 10 ⁺⁰⁸	1.00
	2.752934134304 × 10 ⁻⁰¹	8.702727836448 × 10 ⁺⁰⁰	1.144218965316 × 10 ⁺⁰³	-3.388048706465 × 10 ⁺⁰⁴	4.468226790854 × 10 ⁺⁰⁵	-3.415698564249 × 10 ⁺⁰⁶
	1.63377778876 × 10 ⁻⁰⁷	-4.968757607717 × 10 ⁻⁰⁷	9.345149910740 × 10 ⁻⁰⁷	-9.918132590929 × 10 ⁻⁰⁷	4.54405887417 × 10 ⁻⁰⁷	0.40
	-4.586897364055 × 10 ⁺⁰³	7.410091534510 × 10 ⁺⁰⁴	-5.330157992488 × 10 ⁺⁰⁵	2.248815850944 × 10 ⁺⁰⁶	-6.163267447106 × 10 ⁺⁰⁶	1.146642122359 × 10 ⁺⁰⁷
	-1.466748471041 × 10 ⁺⁰⁷	1.273998992127 × 10 ⁺⁰⁷	-7.192432053384 × 10 ⁺⁰⁶	2.383700014722 × 10 ⁺⁰⁶	-3.522499073032 × 10 ⁺⁰⁵	0.98
	2.404315546780 × 10 ⁻⁰⁴	-8.923341400677 × 10 ⁻⁰⁴	4.612883566157 × 10 ⁻⁰¹	-7.767130012944 × 10 ⁺⁰⁰	5.906199992866 × 10 ⁺⁰¹	-2.510067357691 × 10 ⁺⁰²
	6.444422065762 × 10 ⁺⁰²	-1.021694965030 × 10 ⁺⁰³	9.783366505097 × 10 ⁺⁰²	-5.187127455111 × 10 ⁺⁰²	1.169382345802 × 10 ⁺⁰²	0.96
	-1.773905588902 × 10 ⁺⁰⁷	5.843584501314 × 10 ⁺⁰⁷	-3.653333345290 × 10 ⁺⁰⁷	-4.606281056233 × 10 ⁺⁰⁷	1.619802607015 × 10 ⁺⁰⁷	5.408538264495 × 10 ⁺⁰⁷
	1.621101469014 × 10 ⁻⁰⁷	-5.144098071221 × 10 ⁻⁰⁷	-4.194918461684 × 10 ⁻⁰⁷	7.193648320012 × 10 ⁻⁰⁷	-2.314138629057 × 10 ⁻⁰⁷	0.98
	1.000559287474 × 10 ⁺⁰⁰	6.448389870227 × 10 ⁻⁰¹	-2.393847518557 × 10 ⁺⁰¹	1.795996121322 × 10 ⁺⁰²	-7.983513079578 × 10 ⁺⁰²	2.231880452443 × 10 ⁺⁰³
	-4.022602048469 × 10 ⁺⁰³	4.661556690390 × 10 ⁺⁰³	-3.351063881763 × 10 ⁺⁰³	1.358337273817 × 10 ⁺⁰³	-2.370385908777 × 10 ⁺⁰²	1.00
	4	9.419233225215 × 10 ⁻⁰¹	8	9.773408658583 × 10 ⁻⁰¹		
	5	0.400735600000 × 10 ⁺⁰⁰	0.375837300000 × 10 ⁺⁰⁰	0.002330000000 × 10 ⁺⁰⁰	0.009580000000 × 10 ⁺⁰⁰	
	10	1.503314000000 × 10 ⁺⁰⁰	1.376226000000 × 10 ⁺⁰⁰	0.010300000000 × 10 ⁺⁰⁰	0.036300000000 × 10 ⁺⁰⁰	
	25	8.311198000000 × 10 ⁺⁰⁰	7.329095000000 × 10 ⁺⁰⁰	0.053700000000 × 10 ⁺⁰⁰	0.205800000000 × 10 ⁺⁰⁰	
	T_s	mdot_ethanol	mdot_water	$(d/d_0)^2$	0.0125	400
	7.862289962779 × 10 ⁻⁰¹	-1.905590358774 × 10 ⁻⁰²	8.246785670685 × 10 ⁻⁰¹	-1.189278170599 × 10 ⁺⁰¹	8.651374286353 × 10 ⁺⁰¹	-3.621138473748 × 10 ⁺⁰²
	9.252367142150 × 10 ⁺⁰²	-1.466295075690 × 10 ⁺⁰²	1.406483886905 × 10 ⁺⁰³	-7.478317983028 × 10 ⁺⁰²	1.691842938766 × 10 ⁺⁰²	0.96
	-2.632780788706 × 10 ⁺⁰⁶	8.756215047302 × 10 ⁺⁰⁶	-5.635015992938 × 10 ⁺⁰⁶	-6.830810004370 × 10 ⁺⁰⁶	2.639894271472 × 10 ⁺⁰⁶	8.31213030150 × 10 ⁺⁰⁶
	2.210078937118 × 10 ⁺⁰⁶	-7.857067320592 × 10 ⁺⁰⁶	-6.121967511837 × 10 ⁺⁰⁶	1.089707035414 × 10 ⁺⁰⁷	-3.55628976121 × 10 ⁺⁰⁶	1.00
	1.560434982301 × 10 ⁺⁰⁰	-3.584909539160 × 10 ⁻⁰¹	-1.002599438306 × 10 ⁻⁰¹	9.143432826663 × 10 ⁻⁰¹	-5.07952110053 × 10 ⁻⁰²	1.772075950528 × 10 ⁺⁰³
	-3.976159979558 × 10 ⁺⁰³	5.720137301422 × 10 ⁺⁰³	-5.093793946382 × 10 ⁺⁰³	2.554642949221 × 10 ⁺⁰³	-5.516078934044 × 10 ⁺⁰²	0.96
	-1.019233689173 × 10 ⁺⁰⁸	3.355736007823 × 10 ⁺⁰⁸	-2.095540536280 × 10 ⁺⁰⁸	-2.644960160142 × 10 ⁺⁰⁸	9.271265829597 × 10 ⁺⁰⁷	3.103094381255 × 10 ⁺⁰⁸
	9.324450303629 × 10 ⁻⁰⁷	-2.948950637107 × 10 ⁻⁰⁸	-2.407416453108 × 10 ⁻⁰⁸	4.123432219334 × 10 ⁻⁰⁸	-1.325732748154 × 10 ⁻⁰⁸	0.98
	9.402921380123 × 10 ⁻⁰⁴	-1.994466791369 × 10 ⁻⁰²	6.611844369495 × 10 ⁻⁰¹	-8.797787970135 × 10 ⁺⁰⁰	6.18263992352 × 10 ⁺⁰⁰	-2.542505313592 × 10 ⁺⁰²
	6.434200264873 × 10 ⁺⁰²	-1.014333780203 × 10 ⁺⁰³	9.704339743269 × 10 ⁺⁰²	-5.155566044707 × 10 ⁺⁰²	1.166918331272 × 10 ⁺⁰²	0.96
	-2.924799743519 × 10 ⁺⁰⁷	9.692792220794 × 10 ⁺⁰⁷	-6.137504854373 × 10 ⁺⁰⁷	-7.647925312632 × 10 ⁺⁰⁷	2.785359590473 × 10 ⁺⁰⁷	9.061249660100 × 10 ⁺⁰⁷
	2.639540122732 × 10 ⁺⁰⁷	-8.6972030805188 × 10 ⁺⁰⁷	-7.007536730384 × 10 ⁺⁰⁷	1.21798940888 × 10 ⁺⁰⁸	-3.942133636662 × 10 ⁺⁰⁷	0.98
	1.000050076479 × 10 ⁺⁰⁰	-1.062932595689 × 10 ⁺⁰⁰	7.245769617629 × 10 ⁻⁰¹	-9.798521692955 × 10 ⁺⁰⁰	6.905498511958 × 10 ⁺⁰¹	-2.797130992485 × 10 ⁺⁰²
	6.916110567934 × 10 ⁺⁰²	-1.060807127053 × 10 ⁺⁰³	9.850863108643 × 10 ⁺⁰²	-5.072496164753 × 10 ⁺⁰²	1.11820518397 × 10 ⁺⁰²	1.00
	1	0.156710100000 × 10 ⁺⁰⁰	0.148750100000 × 10 ⁺⁰⁰			
	2	0.595168700000 × 10 ⁺⁰⁰	0.554198100000 × 10 ⁺⁰⁰			
	5	3.407837000000 × 10 ⁺⁰⁰	3.068738000000 × 10 ⁺⁰⁰			
	T_s	mdot_ethanol	mdot_water	$(d/d_0)^2$	0.200	800
	7.855192690555 × 10 ⁻⁰¹	1.838584458814 × 10 ⁺⁰⁰	-1.939381754150 × 10 ⁺⁰¹	1.014231619311 × 10 ⁺⁰²	-2.525476466730 × 10 ⁺⁰²	9.952791292086 × 10 ⁺⁰¹
	1.075057907659 × 10 ⁺⁰³	-2.962036192513 × 10 ⁺⁰³	3.611865130408 × 10 ⁺⁰³	-2.194732350432 × 10 ⁺⁰³	5.393937884827 × 10 ⁺⁰²	0.96
	-6.185737573626 × 10 ⁺⁰⁶	2.017953708989 × 10 ⁺⁰⁷	-1.243901167741 × 10 ⁺⁰⁷	-1.570941653181 × 10 ⁺⁰⁷	5.371475191215 × 10 ⁺⁰⁶	1.811928759723 × 10 ⁺⁰⁷
	5.482737922654 × 10 ⁺⁰⁶	-1.692716034608 × 10 ⁺⁰⁷	-1.379509011181 × 10 ⁺⁰⁷	2.333497911437 × 10 ⁺⁰⁷	-7.431599440408 × 10 ⁺⁰⁶	1.00
	2.437551893200 × 10 ⁻⁰¹	9.383573504797 × 10 ⁺⁰⁰	1.543877298855 × 10 ⁺⁰²	9.118228320071 × 10 ⁺⁰²	-1.145967871160 × 10 ⁺⁰⁵	1.863926378632 × 10 ⁺⁰⁶
	-1.499536169791 × 10 ⁻⁰⁷	6.988466249010 × 10 ⁻⁰⁷	-1.921440765174 × 10 ⁻⁰⁸	2.90143383933 × 10 ⁻⁰⁸	-1.859631243589 × 10 ⁻⁰⁸	0.30
	-7.124197329133 × 10 ⁺⁰¹	1.379566883424 × 10 ⁺⁰³	-1.162476576074 × 10 ⁺⁰⁴	5.705410528614 × 10 ⁺⁰⁴	-1.807399559133 × 10 ⁺⁰⁵	3.862591840428 × 10 ⁺⁰⁵
	-5.641731760705 × 10 ⁺⁰⁵	5.563408619606 × 10 ⁺⁰⁵	-3.546411464371 × 10 ⁺⁰⁵	1.320237741952 × 10 ⁺⁰⁵	-2.180745838176 × 10 ⁺⁰⁴	0.96
	8.150182735870 × 10 ⁺⁰⁶	-2.695515127347 × 10 ⁺⁰⁷	1.709579083723 × 10 ⁺⁰⁷	2.103683809293 × 10 ⁺⁰⁷	-7.767692059457 × 10 ⁺⁰⁶	-2.475081198232 × 10 ⁺⁰⁷
	0.7403391174153 × 10 ⁺⁰⁶	2.357583125696 × 10 ⁺⁰⁷	1.872779798648 × 10 ⁺⁰⁷	-3.257933248603 × 10 ⁺⁰⁷	1.050975806630 × 10 ⁺⁰⁷	1.00
	5.158183206384 × 10 ⁻⁰³	5.052144773312 × 10 ⁻⁰¹	-7.155630553926 × 10 ⁻⁰¹	-3.095923339265 × 10 ⁻⁰¹	2.86028494387 × 10 ⁻⁰²	-1.210039772187 × 10 ⁺⁰³
	2.959010285807 × 10 ⁺⁰³	-4.416309705418 × 10 ⁺⁰³	3.973192996209 × 10 ⁺⁰³	-1.980895625701 × 10 ⁺⁰³	4.204763162322 × 10 ⁺⁰²	0.90
	-1.536378626823 × 10 ⁺⁰⁷	7.710523562694 × 10 ⁺⁰⁷	-1.219828904231 × 10 ⁺⁰⁸	1.32757682698 × 10 ⁺⁰⁷	1.171145827961 × 10 ⁺⁰⁸	-7.124952058481 × 10 ⁺⁰⁶
	-1.339786977567 × 10 ⁺⁰⁸	-2.064156773762 × 10 ⁺⁰⁶	1.769124067650 × 10 ⁺⁰⁸	-1.361571147800 × 10 ⁺⁰⁸	3.226357686589 × 10 ⁺⁰⁷	0.98
	-1.931978544127 × 10 ⁺⁰⁵	3.970437400385 × 10 ⁺⁰⁵	6.114688294366 × 10 ⁺⁰⁴	-2.756380153123 × 10 ⁺⁰⁵	-2.725084802087 × 10 ⁺⁰⁵	6.974234266885 × 10 ⁺⁰³
	2.870410001606 × 10 ⁺⁰⁵	2.837685708678 × 10 ⁺⁰⁵	-7.902788571659 × 10 ⁺⁰⁴	-4.423583453077 × 10 ⁺⁰⁵	2.267561527146 × 10 ⁺⁰⁵	1.00
	9.976420896304 × 10 ⁻⁰¹	4.692846983512 × 10 ⁻⁰¹	-1.648966737344 × 10 ⁺⁰¹	1.033136121470 × 10 ⁺⁰²	-3.871833168029 × 10 ⁺⁰²	9.074919704247 × 10 ⁺⁰²
	-1.339729551873 × 10 ⁺⁰³	1.209796161179 × 10 ⁺⁰³	-6.107918394416 × 10 ⁺⁰²	1.330733405877 × 10 ⁺⁰²	-7.419910249997 × 10 ⁻⁰¹	1.00
	4	9.964083311610 × 10 ⁻⁰¹	8	9.972790618083 × 10 ⁻⁰¹		
	5	0.633801000000 × 10 ⁺⁰⁰	0.580001000000 × 10 ⁺⁰⁰	9.866199000000 × 10 ⁺⁰⁰	34.959999000000 × 10 ⁺⁰⁰	
	10	2.320001000000 × 10 ⁺⁰⁰	2.059901000000 × 10 ⁺⁰⁰	34.589999000000 × 10 ⁺⁰⁰	111.440099000000 × 10 ⁺⁰⁰	
	25	12.310050000000 × 10 ⁺⁰⁰	10.520050000000 × 10 ⁺⁰⁰	177.690050000000 × 10 ⁺⁰⁰	429.479950000000 × 10 ⁺⁰⁰	
	T_s	mdot_ethanol	mdot_water	$(d/d_0)^2$	0.200	1200
	7.845309427488 × 10 ⁻⁰¹	2.370679345354 × 10 ⁺⁰⁰	-2.490086336832 × 10 ⁺⁰¹	1.270988572169 × 10 ⁺⁰²	-2.935275698215 × 10 ⁺⁰²	-1.004054362685 × 10 ⁺⁰¹
	1.728219025810 × 10 ⁺⁰³	-4.327089095261 × 10 ⁺⁰³	5.104106989917 × 10 ⁺⁰³	-3.044262366896 × 10 ⁺⁰³	7.384879679082 × 10 ⁺⁰²	0.96
	-5.854194548888 × 10 ⁺⁰⁶	1.914222913185 × 10 ⁺⁰⁷	-1.185631674012 × 10 ⁺⁰⁷	-1.490884575436 × 10 ⁺⁰⁷	5.164373888153 × 10 ⁺⁰⁶	1.725266648586 × 10 ⁺⁰⁷
	5.169625765463 × 10 ⁺⁰⁶	-1.161899062531 × 10 ⁺⁰⁷	-1.312223578000 × 10 ⁺⁰⁷	2.229745750862 × 10 ⁺⁰⁷	-7.115852017365 × 10 ⁺⁰⁶	1.00
	1.382051357139 × 10 ⁻⁰¹	7.934434006405 × 10 ⁺⁰⁰	-4.741032640278 × 10 ⁺⁰¹	1.411709408340 × 10 ⁺⁰⁴	-3.543175089794 × 10 ⁺⁰⁵	4.553170480702 × 10 ⁺⁰⁶
	-3.31756091007 × 10 ⁻⁰⁷	1.463740008506 × 10 ⁻⁰⁸	-3.885849698733 × 10 ⁻⁰⁸	5.724934174109 × 10 ⁻⁰⁸	-3.602142480115 × 10 ⁻⁰⁸	0.30
	-1.251805075437 × 10 ⁺⁰²	2.394939408786 × 10 ⁺⁰³	-2.008584833515 × 10 ⁺⁰⁴	9.810361490887 × 10 ⁺⁰⁴	-3.091412549280 × 10 ⁺⁰⁵	6.568937027490 × 10 ⁺⁰⁵
	-9.53534375929 × 10 ⁺⁰⁵	9.340961704319 × 10 ⁺⁰⁵	-5.912397148592 × 10 ⁺⁰⁵	2.184592841669 × 10 ⁺⁰⁵	-3.580263826150 × 10 ⁺⁰⁴	0.96
	-2.411516746177 × 10 ⁺⁰⁶	7.373941988366 × 10 ⁺⁰⁶	-3.902809970567 × 10 ⁺⁰⁶	-5.668520727874 × 10 ⁺⁰⁶	1.171614126754 × 10 ⁺⁰⁶	5.888020968782 × 10 ⁺⁰⁶
	2.375092084350 × 10 ⁺⁰⁶	-4.897996663699 × 10 ⁺⁰⁶	-4.636914987621 × 10 ⁺⁰⁶	6.649476059941 × 10 ⁺⁰⁶	-1.940386131946 × 10 ⁺⁰⁶	1.00

3. Gao, F.; Xu, Z.; Zhao, H. Flame spray pyrolysis made Pt/TiO₂ photocatalysts with ultralow platinum loading and high hydrogen production activity. *Proc. Combust. Inst.* **2021**, *38*, 6503–6511. [[CrossRef](#)]
4. Deligiannakis, Y.; Tsikourkitoudi, V.; Stathi, P.; Wegner, K.; Papavasiliou, J.; Louloudi, M. PdO/Pd⁰/TiO₂ nanocatalysts engineered by flame spray pyrolysis: Study of the synergy of PdO/Pd⁰ on H₂ production by HCOOH dehydrogenation and the deactivation mechanism. *Energy Fuels* **2020**, *34*, 15026–15038. [[CrossRef](#)]
5. Yuan, X.; Meng, L.; Xu, Z.; Zheng, C.; Zhao, H. CuO quantum dots supported by SrTiO₃ perovskite using the flame spray pyrolysis method: Enhanced activity and excellent thermal resistance for catalytic combustion of CO and CH₄. *Environ. Sci. Technol.* **2021**, *55*, 14080–14086. [[CrossRef](#)]
6. Yuan, X.; Zheng, C.; Zhao, H. Photothermocatalytic removal of CO and formaldehyde with excellent water vapor stability over dual-functional copper loading on TiO₂ synthesized via flame spray pyrolysis. *Sol. RRL* **2021**, *5*, 2100490. [[CrossRef](#)]
7. Meierhofer, F.; Mädler, L.; Fritsching, U. Nanoparticle evolution in flame spray pyrolysis—Process design via experimental and computational analysis. *AIChE J.* **2020**, *66*, e16885. [[CrossRef](#)]
8. Dasgupta, D.; Pal, P.; Torelli, R.; Som, S.; Paulson, N.; Libera, J.; Stan, M. Computational fluid dynamics modeling and analysis of silica nanoparticle synthesis in a flame spray pyrolysis reactor. *Combust. Flame* **2022**, *236*, 111789. [[CrossRef](#)]
9. Madero, J.E.; Li, J.; Shen, K.Y.; Wojtak, J.; Axelbaum, R.L. An approach to low-temperature flame spray pyrolysis for the synthesis of temperature-sensitive materials: Application to Li_{1.2}Mn_{0.54}Ni_{0.13}Co_{0.13}O₂. *Appl. Energy Combust. Sci.* **2021**, *5*, 100020. [[CrossRef](#)]
10. Paulson, N.H.; Libera, J.A.; Stan, M. Flame spray pyrolysis optimization via statistics and machine learning. *Mater. Des.* **2020**, *196*, 108972. [[CrossRef](#)]
11. Schneider, F.; Suleiman, S.; Menser, J.; Borukhovich, E.; Wlokas, I.; Kempf, A.; Wiggers, H.; Schulz, C. SpraySyn—A standardized burner configuration for nanoparticle synthesis in spray flames. *Rev. Sci. Instrum.* **2019**, *90*, 085108. [[CrossRef](#)] [[PubMed](#)]
12. Suleiman, S.; Nanjaiah, M.; Skenderovic, I.; Rosenberger, T.; Kunze, F.; Wlokas, I.; Kruis, E.; Wiggers, H.; Schulz, C. Atmospheric-pressure particle mass spectrometer for investigating particle growth in spray flames. *J. Aerosol Sci.* **2021**, *158*, 105827. [[CrossRef](#)]
13. Stodt, M.F.; Liu, C.; Li, S.; Mädler, L.; Fritsching, U.; Kiefer, J. Phase-selective laser-induced breakdown spectroscopy in flame spray pyrolysis for iron oxide nanoparticle synthesis. *Proc. Combust. Inst.* **2021**, *38*, 1711–1718. [[CrossRef](#)]
14. Tischendorf, R.; Simmler, M.; Weinberger, C.; Bieber, M.; Reddemann, M.; Fröde, F.; Lindner, J.; Pitsch, H.; Kneer, R.; Tiemann, M.; et al. Examination of the evolution of iron oxide nanoparticles in flame spray pyrolysis by tailored in situ particle sampling techniques. *J. Aerosol Sci.* **2021**, *154*, 105722. [[CrossRef](#)]
15. Majerič, P.; Rudolf, R. Advances in ultrasonic spray pyrolysis processing of noble metal nanoparticles. *Materials* **2020**, *13*, 3485. [[CrossRef](#)] [[PubMed](#)]
16. Dasgupta, D.; Pal, P.; Torelli, R.; Som, S. Computational fluid dynamics modeling of flame spray pyrolysis for nanoparticle synthesis. In Proceedings of the 2020 Spring Technical Meeting of the Central States Section of the Combustion Institute, Huntsville, AL, USA, 17–19 May 2020.
17. Rittler, A.; Deng, L.; Wlokas, I.; Kempf, A. Large eddy simulations of nanoparticle synthesis from flame spray pyrolysis. *Proc. Combust. Inst.* **2017**, *36*, 1077–1087. [[CrossRef](#)]
18. Neto, P.B.; Meierhofer, F.; Meier, H.F.; Fritsching, U.; Noriler, D. Modelling polydisperse nanoparticle size distributions as produced via flame spray pyrolysis. *Powder Technol.* **2020**, *370*, 116–128. [[CrossRef](#)]
19. Widiyastuti, W.; Wang, W.N.; Lenggono, I.W.; Iskandar, F.; Okuyama, K. Simulation and experimental study of spray pyrolysis of polydispersed droplets. *J. Mater. Res.* **2007**, *22*, 1888–1898. [[CrossRef](#)]
20. Gopale, D.L.; Arote, S.A.; Borse, R.Y. Mathematical modeling of droplet formation, evaporation, and film growth to study crystallite size and film thickness of spray pyrolysis deposited TiO₂ thin films. *e-J. Surf. Sci. Nanotechnol.* **2018**, *16*, 419–426. [[CrossRef](#)]
21. Narasu, P.; Keller, A.; Kohns, M.; Hasse, H.; Gutheil, E. Numerical study of the evaporation and thermal decomposition of a single iron (III) nitrate nonahydrate/ethanol droplet. *Int. J. Therm. Sci.* **2021**, *170*, 107133. [[CrossRef](#)]
22. Brenn, G.; Deviprasath, L.; Durst, F.; Fink, C. Evaporation of acoustically levitated multi-component liquid droplets. *Int. J. Heat Mass Transf.* **2007**, *50*, 5073–5086. [[CrossRef](#)]
23. Narasu, P.; Boschmann, S.; Pöschko, P.; Zhao, F.; Gutheil, E. Modeling and simulation of single ethanol/water droplet evaporation in dry and humid air. *Combust. Sci. Technol.* **2020**, *192*, 1233–1252. [[CrossRef](#)]
24. Abramzon, B.; Sirignano, W. Droplet vaporization model for spray combustion calculations. *Int. J. Heat Mass Transfer* **1989**, *32*, 1605–1618. [[CrossRef](#)]
25. Mu, J.; Perlmutter, D. Thermal decomposition of metal nitrates and their hydrates. *Thermochim. Acta* **1982**, *56*, 253–260. [[CrossRef](#)]
26. Law, C.K. Recent advances in droplet vaporization and combustion. *Prog. Energy Combust. Sci.* **1982**, *8*, 171–201. [[CrossRef](#)]
27. Narasu, P.; Nanjaiah, M.; Wlokas, I.; Gutheil, E. Numerical simulation and parameterization of the heating and evaporation of a titanium(IV) isopropoxide/p-xylene precursor/solvent droplet in hot convective air. *Int. J. Multiph. Flow* **2022**, *150*, 104006. [[CrossRef](#)]
28. Keller, A.; Wlokas, I.; Kohns, M.; Hasse, H. Thermophysical properties of solutions of iron (III) nitrate nonahydrate in mixtures of ethanol and water. *J. Chem. Eng. Data* **2020**, *65*, 3519–3527. [[CrossRef](#)]